Irreversible Anion Oxidation Leads to Dynamic Charge Compensation in Ru-poor, Li-rich Cathode $Li_2Ru_{0.3}Mn_{0.7}O_3$

Joshua J. Zak,[†] Mateusz Zuba,[‡] Zachary W. Lebens-Higgins,[‡] Heran Huang,[‡] Matthew J. Crafton,[¶] Nathan F. Dalleska,[§] Bryan D. McCloskey,[¶] Louis F. J. Piper,[‖,‡] and Kimberly A. See[*,†]

[†]*Division of Chemistry and Chemical Engineering, California Institute of Technology, Pasadena, California 91125, United States*

[‡]*Department of Physics, Applied Physics and Astronomy, Binghamton University, Binghamton, New York 13902, United States*

[¶]*Department of Chemical and Biomolecular Engineering, University of California, Berkeley, California 94720, United States*

[§]*Division of Geological and Planetary Sciences, California Institute of Technology, Pasadena, California 91125, United States*

[‖]*WMG, University of Warwick, Coventry CV4 7AL, United Kingdom*

E-mail: ksee@caltech.edu

Abstract

Conventional cathodes for Li-ion batteries are layered transition metal oxides that support Li^+ intercalation charge-balanced by redox on the transition metals. Oxidation beyond one electron per transition metal can be achieved in Li-rich layered oxides by involving structural anions, which necessitates high voltages and complex charge compensation mechanisms convoluted by degradation reactions. We report a detailed structural and spectroscopic analysis of the multielectron material $Li_2Ru_{0.3}Mn_{0.7}O_3$, chosen due to low Ru content. *Ex situ* and *operando* spectroscopic data over multiple cycles highlight the changing charge compensation mechanism. Notably, over half of the first cycle capacity is attributed to O_2 gas evolution and reversible O redox is minimal. Instead, reduced Ru and Mn species are detected in the bulk and on the surface, which then increasingly contribute to charge compensation as more metal reduction occurs with cycling. Permanent structural changes linked to metal migration are observed with EXAFS and Raman analysis.

Main Text

In recent years, Li-rich oxides have been the subject of fervent investigation as high-capacity cathodes for Li-ion batteries (LIBs).[1–6] Many examples take advantage of high-voltage processes most often attributed to oxidation of structural anions, going beyond the one electron per transition metal paradigm under which virtually all commercial LIB cathode materials operate.[7] The Li-rich material Li_2MnO_3, which is a component of Li-rich NMC materials,[8] was once thought to be electrochemically inactive.[9] Activation of Li_2MnO_3 can be achieved by nanoscaling the particles,[10] but the capacity ~~was~~ is attributed primarily to irreversible side reactions involving the electrolyte, native surface carbonates, and gas evolution.[11] Thus, other materials in the Li_2MO_3 materials

family have been explored to leverage the high Li to metal ratio. In particular, the focus has been on tuning the metal-anion covalency to access both cation and anion redox by changing the transition metal to 4d and 5d metals.[12–15]

One such 5d metal oxide is Li_2RuO_3, first reported by Goodenough and coworkers.[16] Li_2RuO_3 shows high gravimetric capacity with charge compensation suggested from both Ru and O redox.[17] However, Ru is a prohibitively expensive metal, which led to substitution of Ru in Li_2RuO_3 with less precious metals like Sn,[13] Ti,[18] and Mn.[12,19] The solid solution between Li_2RuO_3 and Li_2MnO_3 is of interest due to the body of knowledge already ~~accummulated~~ accumulated on the electrochemical behavior of Li_2MnO_3, both on its own and as a component of Li-rich NMC materials. Sathiya *et al.* first reported the $Li_2Ru_{1-y}Mn_yO_3$ solid solution and more deeply characterized the $y = 0.4$ member, $Li_2Ru_{0.6}Mn_{0.4}O_3$.[12] Similarly, Lyu *et al.* focused on the $Li_2Ru_{0.5}Mn_{0.5}O_3$ material and examined the redox behavior and structural response to (de)lithiation over a wide voltage window.[19] These analyses of the $Li_2Ru_{1-y}Mn_yO_3$ solid solution focus on the more Ru-rich materials. Also, exploring the materials with a significantly lower voltage cutoff as in Lyu *et al.* make comparisons between materials and reports difficult.[19] Reducing the amount of Ru in the structure is important for cost reasons, and exploring if the same rules apply to Ru-poor materials is imperative to understand the role of Ru and probe the effects on anion redox mechanisms. Here, we aim to address several questions: (1) What are the contributions of each redox-active component and how does that evolve over time? (2) Are the bulk and surface processes the same or different? (3) How ~~does the structural response to redox influence reversibility~~are these mechanisms generalizable to other materials systems? As such, we report the detailed characterization of the charge compensation mechanism and consequent structural response to (de)lithiation for ~~Ru-poor~~ Mn-rich material $Li_2Ru_{0.3}Mn_{0.7}O_3$. We find a complex and dynamic redox mechanism, the ~~deconvolution of which~~ comparison of which to similar chemistries like Li- and Mn-rich NMCs provides insight into ~~anion redox mechanisms in similar Li-rich layered oxide~~ the efficacy of a materials development approach based on tuning the electronic structure, i.e. metal-anion covalency, in next-generation cathodes.

As-synthesized Li_2RuO_3 and Li_2MnO_3 are black and bright orange, respectively, due to the intrinsic differences in electronic structure dictated by the transition metal. Li_2RuO_3 is a semimetal[20] and Li_2MnO_3 is a wide-bandgap semiconductor.[21] Detailed characterization is conducted on $Li_2Ru_{0.3}Mn_{0.7}O_3$ as a low-Ru material that exhibits multielectron storage capabilities with respect to the transition metal content yielding over 250 mAh g^{-1} on the first charge (1.2 mol e^- per f.u.). $Li_2Ru_{0.3}Mn_{0.7}O_3$ is a dark brown powder, a visual sign that the material is well-mixed. The X-ray diffraction (XRD) pattern with quantitative Rietveld refinement is shown in Figure S1. Sathiya *et al.* previously reported the structure and refined lattice parameters of several materials in the solid solution[12] but did not report the Ru = 0.3 material. Here, we find that $Li_2Ru_{0.3}Mn_{0.7}O_3$ crystallizes in the $C2/m$ space group of Li_2MnO_3. Like in previous reports of similar materials,[12,19] the XRD pattern was fit by allowing intraplanar site mixing in the LiM_2 layers between the 4g and 2b sites occupied by a transition metal and Li, respectively. The refinement is adequate to show that the phase is formed but it does not describe the peaks between 20 and 34° 2θ attributed to Li/transition metal ordering in the layers, thus signifying significant disorder in the assumed O3 stacking of $Li_2Ru_{0.3}Mn_{0.7}O_3$.[22,23] This is likely due to mixing on the 4g and 2b sites by Li, Ru, and Mn. If intralayer mixing is not allowed, the refinement fits slightly worse as evidenced by a higher residual value (Figure S2). The stoichiometry is supported by a comparison of *ex situ* Raman spectra of various materials in the $Li_2Ru_{1-y}Mn_yO_3$ ($y > 0.4$) solid solution (Figure S3) in which there are systematic changes to the spectra as Ru content is increased. The peaks broaden as disorder increases and two new Ru-related modes appear around 680 and 720 cm^{-1}.

The galvanostatic cycling data is shown in Figure 1a. $Li_2Ru_{0.3}Mn_{0.7}O_3$ exhibits charge storage capabilities greater than that afforded by $Ru^{4+/5+}$ redox alone, which would give only ~~approximately~~ 62 mAh g^{-1}. ~~However, the~~ The extent to which the extra capacity is contributed by redox on

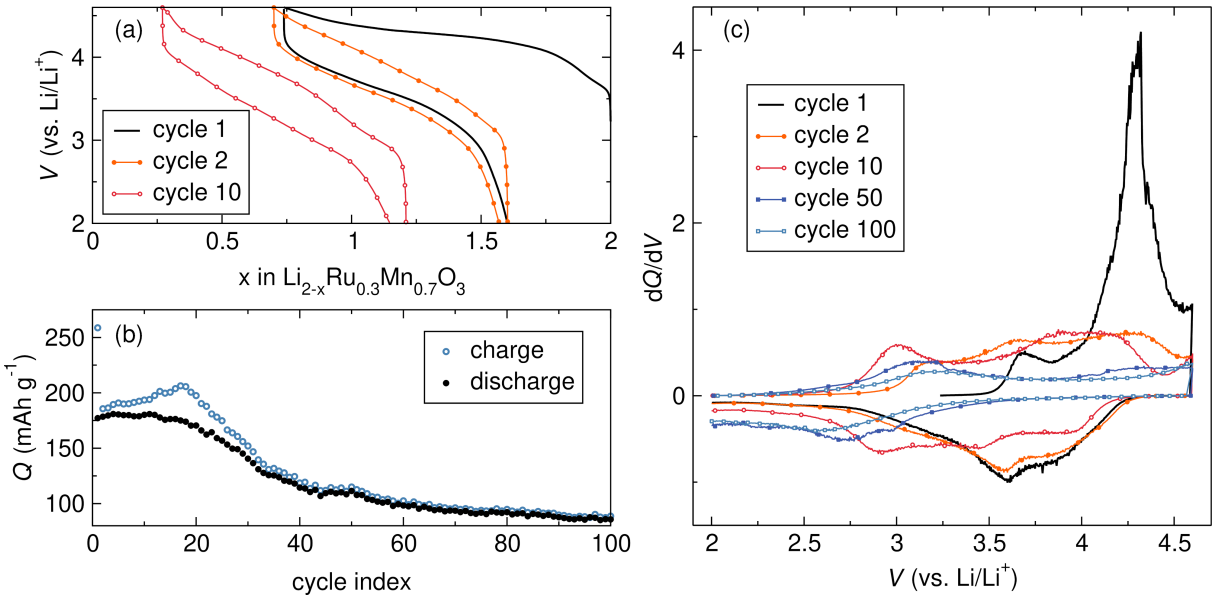

Figure 1: (a) Charge and discharge profiles from cycles 1, 2, and 10, (b) long-term cycling performance of $Li_2Ru_{0.3}Mn_{0.7}O_3$ at a rate of C/10 based on 1 e^- per formula unit, and (c) differential capacity (dQ/dV) plot of $Li_2Ru_{0.3}Mn_{0.7}O_3$ from selected cycles.

the oxide anions or by side reactions is an important distinction. ~~We assert that the redox mechanisms in this material are complex and change throughout cycling, and a detailed account of the charge compensation mechanism is laid out in the following discussion.~~ The voltage profile shows an initial sloping region with an inflection around 3.75 V followed by a more gently sloping plateau centered around 4.2 V. The subsequent discharge is S-shaped with a significant voltage hysteresis and an irreversible capacity loss of approximately 82 mAh g^{-1}, consistent with previous reports.[12,19] After extended cycling, the voltage profile shows evidence of two more distinct sloping regions centered around 3.2 V and 4.3 V and greater voltage hysteresis, and the full set of cycling data is shown in Figure S4. The evolution of the voltage profile with cycling suggests significant changes to the charge compensation mechanism over time. The long-term cycling performance of $Li_2Ru_{0.3}Mn_{0.7}O_3$ is shown in Figure 1b. Interestingly, the capacity upon charging increases steadily from 186 mAh g^{-1} to 206 mAh g^{-1} between cycles 2 and 18 before beginning to decrease. While the capacity during charge increases, the capacity during discharge does not indicating some irreversibility in the charging mechanism during oxidation. Furthermore, when the charge capacity starts decreasing after cycle 18 the discharge capacity decreases as well, suggesting that the irreversible processes contributing to the initial increase of the capacity during charge are self-terminating. Additional details on hypotheses to explain this behavior are presented below.

The differential capacity curves shown in Figure 1c begin to shed light on potential reasons for the odd cycling behavior. The first charge is characterized by a large feature centered around 4.3 V that is not reproduced on later cycles, and the reduction features on discharge are distinctly different than those on charge highlighting the change in mechanism. On later cycles, a new, low-voltage redox couple around 2.8 V (reduction) and 3.2 V (oxidation) appears, and a similar feature in analogous materials has been attributed to Mn redox.[12,24–26] Reduction of surface Mn that then contributes to redox on subsequent cycles ~~could~~ would explain the rise in capacity from cycle 2 to 18. In later cycles, the Mn redox feature begins to disappear along with the higher voltage features, which explains the more rapid decrease in capacity after cycle 18 and corroborates a changing charge compensation mechanism.

To explore the origins of the excess capacity beyond $Ru^{4+/5+}$, we first employ a variety of bulk characterization techniques on extracted elec-

trodes at different states of charge (SOCs) in cycles 1, 2, and 10. First, evidence of the changes to the oxidation state of Ru and Mn are elucidated through K-edge X-ray absorption spectroscopy (XAS). Cycle 1 and cycle 2 are hereafter compared due to the significant change in the electrochemistry after the first charge, and data from cycle 10 is used to probe for changes that evolve with cycling.

The Ru K-edge spectra of $Li_2Ru_{0.3}Mn_{0.7}O_3$ are shown in Figure 2a-d. The rising edge position, here defined as the energy at half the height of the main absorption edge, is 22129.5 eV corresponding to bulk Ru^{4+} ~~in reasonable agreement with~~ . The rising edge position of $Li_2Ru_{0.3}Mn_{0.7}O_3$ is approximately 1 eV higher than that reported for $Li_2Ru_{0.5}Mn_{0.5}O_3$.[19] ~~Compared to reports of similar materials like~~ [19] and similar material $Li_{1.2}Ni_{0.2}Ru_{0.6}O_2$, ~~which adopts the $R\bar{3}m$ structure like $LiCoO_2$,~~[27] ~~the rising edge position of $Li_2Ru_{0.3}Mn_{0.7}O_3$ is approximately 1 eV higher~~[27] , suggesting that the Ru–O interaction is more ionic.[28] The lower proportion of Ru compared to the 3d metal causes greater isolation of Ru, likely contributing to the greater degree of charge localization in $Li_2Ru_{0.3}Mn_{0.7}O_3$. Upon charging to 4.15 V, the rising edge position shifts to higher energy by 0.5 eV, which indicates oxidation of bulk Ru^{4+} to Ru^{5+}. At 4.15 V, the charge passed as measured by the electrochemistry equates to almost exactly that required to oxidize all Ru to Ru^{5+} (61.5 mAh g^{-1}). Upon fully charging to 4.6 V, the rising edge does not shift further, suggesting oxidation of Ru does not proceed past Ru^{5+}. At full SOC, the pre-edge region around 22120 eV exhibits an intensity increase, indicating a distortion in the octahedral symmetry as shown in Figure S5, which leads to more efficient d-p mixing.[29] Upon discharging to 2 V, a significant shift (2.2 eV) of the rising edge to lower energy is observed. The shift to lower energies relative to the as-prepared sample indicates an over-reduction of Ru and the presence of Ru^{3+}. Over-reduction is not observed in end member Li_2RuO_3 upon discharge to the same voltage,[30] and, although Ru is over-reduced in $Li_2Ru_{0.5}Mn_{0.5}O_3$,[19] the magnitude of the edge shift below that of the as-prepared material is significantly less than in this work. The immediate over-reduction of Ru is contrary to the more gradual over-reduction of Mn and Co in certain Li- and Mn-rich NMCs.[31,32] Here, after the first discharge, Ru instead begins to act more like Ni does in Li- and Mn-rich NMC materials in that it cycles on a two-electron redox couple ($Ru^{3+/5+}$ vs. $Ni^{2+/4+}$) and the high-valent states have significant covalency with O 2p states. Near-edge scattering features differ slightly in their position and intensity, which points to irreversible changes in the local structure around Ru. The Ru K-edge X-ray absorption near-edge structure (XANES) spectra for the second and tenth cycles display similar trends as the first. Notably, the edge position never recovers to that of the as-prepared material, suggesting that either the average oxidation state of Ru stays lower than 4+ or structural changes lead to new Ru environments. The latter is more likely as the cathode is reaching potentials at which $Ru^{4+/5+}$ oxidation is expected. Figure 2d shows relative changes of the edge position, making apparent the over-reduction of Ru after the first charge process. On later cycles, the edge position never recovers the original value but continues to shift as evidence of Ru involvement in the redox.

Mn K-edge XAS (Figure 2e-h) is also measured to investigate redox non-innocence as suggested by the new low-voltage redox couple observed in the dQ/dV plots. The pre-edge features arise from a 1s to 3d transition for Mn in an octahedral geometry and represent the partially filled t_{2g} (6541 eV) and e_g (6543 eV) states (Figure S6). The edge position of $Li_2Ru_{0.3}Mn_{0.7}O_3$ is 6557 eV, which is in good agreement with reports of Mn K-edge XANES of $Li_2Ru_{0.5}Mn_{0.5}O_3$ [19] and Li_2MnO_3 [11] signifying that Mn is formally Mn^{4+}. The K-edge white line arises from the 1s to 4p transition and is especially sharp and intense due, in part, to the negatively charged neighboring anions and the localization of the excited electron on Mn, suggesting a fairly ionic Mn-O interaction. The rising edge in the Mn K-edge XANES does not shift upon charging, which is more easily observed in Figure 2h, indicating no oxidation of Mn past Mn^{4+}. Irreversible changes to the spectral shape and pre-edge may be due to changes to the local environment around Mn that persist after the first oxidation. After discharging to 2 V, extra spectral weight near the edge at

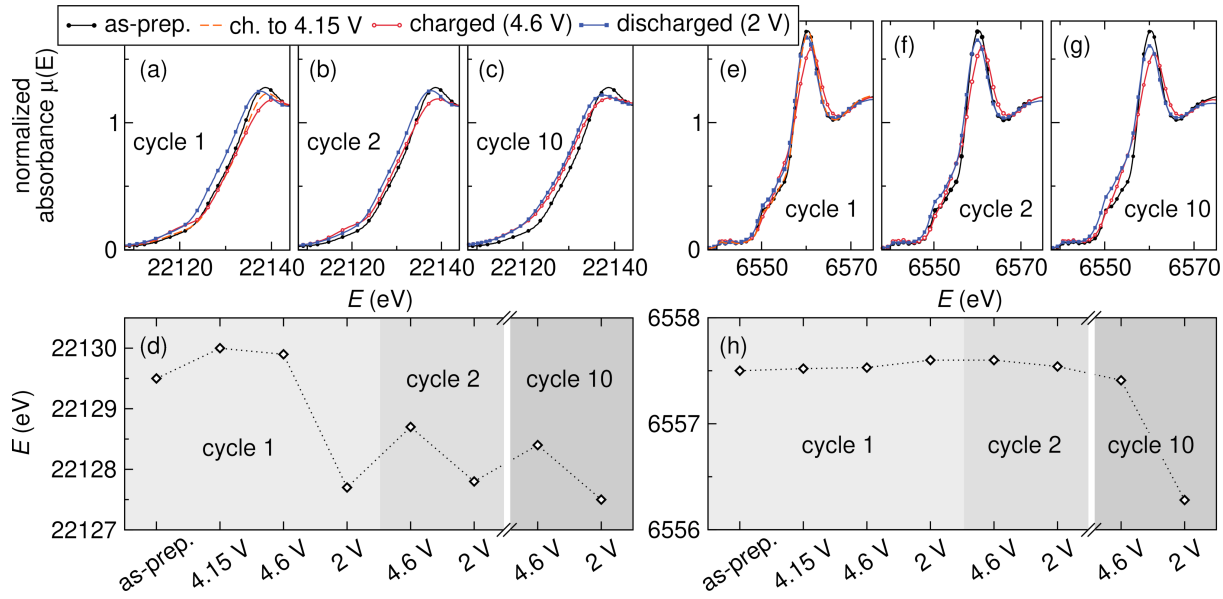

Figure 2: (a-c) *Ex situ* Ru K-edge XANES of $Li_2Ru_{0.3}Mn_{0.7}O_3$ at various SOCs: as-prepared, charged to 4.15 V, charged to 4.6 V, fully charged then discharged to 2 V, charged to 4.6 V on cycle 2, discharged on cycle 2, charged to 4.6 V on cycle 10, and discharged on cycle 10. (d) The change in the Ru K-edge position with cycling highlighting redox involvement and over-reduction upon discharge. (e-g) *Ex situ* Mn K-edge XANES at the same SOC with arrows highlighting reduced Mn. (h) The change in the Mn K-edge position showing minimal changes until later cycles.

lower energies indicates reduction of Mn below Mn^{4+}. The trends are essentially identical in cycle 2. By cycle 10, the edge position decreases by over 1 eV upon discharge, indicating significant Mn involvement to the redox and corroborating the dQ/dV results. This behavior is in line with reports in Li- and Mn-rich NMC materials,[refs] and, interestingly, here Ru acts in much the same ways as Mn and Co when over-reduced to Mn^{3+} and Co^{2+}.[32] After over-reduction, the covalency with buried O states decreases and the transition metals are preferentially oxidized on subsequent cycles leading to voltage fade. However, significant over-reduction of Ru occurs on the first discharge, which leads to immediate changes to the voltage profile. After a while, enough Mn has been gradually reduced to cause further changes as described above.

On the first charge, XAS shows that Ru^{4+} is oxidized and the Mn^{4+} is largely redox innocent in the bulk. However, the charge expected from full oxidation of Ru^{4+} to Ru^{5+} is insufficient to explain the high capacities observed. The possible explanations for the excess capacity are lattice O redox and decomposition reactions, both of which have been reported extensively.[12,19,33,34] To explore the possibility of reversible lattice O redox, O K-edge resonant inelastic X-ray scattering (RIXS) studies are performed. RIXS acts as a sensitive probe of the electronic structure of lattice O by combining XAS and X-ray emission spectroscopy (XES), allowing filled states to be probed and introducing a higher dimensionality than either technique alone.[29] The RIXS maps for $Li_2Ru_{0.3}Mn_{0.7}O_3$ on the first charge are shown in Figure S7. Two pre-edge features are observed and attributed to hybridized Mn 3d–O 2p orbitals split into t_{2g} and e_g states by the octahedral crystal field.[35] The appearance of a RIXS loss feature at 523.5 eV from an excitation at 531 eV has been attributed to bulk O redox contributions in several Li-rich layered oxide systems.[28,36–38] However, this spectroscopic signature is not observed in the RIXS maps of $Li_2Ru_{0.3}Mn_{0.7}O_3$, indicating the lack of bulk O redox activity, a different O oxidation mechanism, or the prevalence of oxidized O being lower than the detection limit in the RIXS measurements. Bruce and coworkers have shown in several closely related systems that high-resolution RIXS is necessary to detect the presence of holes

on O or trapped molecular O_2.[39–41] ~~In the absence of evidence of bulk O redox, we turned to more surface sensitive methods. Figure S8 shows the O K-edge XAS spectra in surface-sensitive total electron yield (TEY) mode. The two pre-edge features at 529.9 and 532.1 eV correspond with the Mn–O hybridized states as observed in the RIXS . An additional feature in the as-prepared sample around 534 eV is attributed to surface carbonates.[51,52] The carbonate feature disappears upon charging suggesting that the carbonates are oxidized off the surface. The changes upon charging consist solely of broadening of the pre-edge features, as is also observed in the RIXS maps, and do not indicate significant oxidation of lattice O that stays near the surface.~~

~~To determine if~~

The lack of RIXS feature corresponding to stable oxidized lattice O prompts investigation into whether irreversible decomposition reactions ~~are occuring,~~ occur, so we turn to differential electrochemical mass spectrometry (DEMS) to characterize gaseous products during cycling. The *operando* DEMS data for the first three cycles are shown in Figure 3a. During the first charge cycle, a significant feature from O_2 gas release is observed starting at the onset of the high-voltage plateau. ~~O_2 release can come from oxidation of lattice O followed by gas release[13,46,47] since~~ Since electrolyte degradation and oxidation of surface carbonates ~~produces exclusively CO_2.~~exclusively produces CO_2,[33,45,48] O_2 formation is primarily attributed to irreversible oxidation of lattice O.[13,46,47] A comparatively small amount of CO_2 is observed at the top of charge (>4.4 V). By integrating the DEMS data, the charge contributions of the decomposition reactions resulting in gaseous products to the total capacity are calculated. The capacity from oxidation to O_2 alone during the first charge assuming a four-electron oxidation process is 122 mAh g^{-1}, or 45.7% of the total charge capacity. Comparatively, CO_2 only contributes approximately 2 mAh g^{-1}. As such, about half of the first charge capacity can be attributed to irreversible degradation reactions. Upon discharging, the gas release drops precipitously, confirming that the gases detected are a result of oxidative decomposition reactions at high voltages. The O_2 gas release on subsequent cycles sequentially decreases ~~.~~ while the CO_2 released stays relatively constant, which may indicate continued decomposition of the electrolyte on the surface. This may provide another explanation to the rising charge capacity between cycles 2 and 18 (Figure 1b), which could eventually hit a point where the electrolyte can no longer decompose on the particle surface perhaps due to coverage by an interphase layer. The gas release ~~likely~~ on the first cycle likely triggers a structural change and consequent change to the redox mechanism, which is corroborated by the change in the shape of the voltage profile.

The release of O_2 from the cathode suggests O^{2-} oxidation and necessitates charge compensation and/or densification near the surface where O vacancies are known to form.[49,50] To probe the effects of gas release and a dynamic charge compensation mechanism on $Li_2Ru_{0.3}Mn_{0.7}O_3$, surface-sensitive probes of the electronic structure including hard X-ray photoelectron spectroscopy (HAXPES) and XAS in total electron yield (TEY) mode are used (Figure 3). Figure S8 shows the O K-edge XAS spectra in surface-sensitive total electron yield (TEY) mode. The two pre-edge features at 529.9 and 532.1 eV correspond with the Mn–O hybridized states as observed in the RIXS. An additional feature in the as-prepared sample around 534 eV is attributed to surface carbonates.[51,52] The carbonate feature disappears upon charging suggesting that the carbonates are oxidized off the surface. The changes upon charging consist solely of broadening of the pre-edge features, as is also observed in the RIXS maps, and do not indicate significant oxidation of lattice O that stays near the surface.In the O 1s region of the HAXPES, the as-prepared $Li_2Ru_{0.3}Mn_{0.7}O_3$ cathode has two main features: a narrow peak around 529.5 eV and a broader feature centered around 532.5 eV attributed to bulk O^{2-} and surface carbonates, respectively.[4,12,53,54] Upon charging to 4.15 V, the feature at 532.5 eV largely disappears as native surface carbonates are oxidized. Then, at full charge, a new feature around 531 eV grows along with additional spectral weight between 532 and 535 eV. The new feature at 531 eV has historically been used as a direct indicator of bulk O oxidation.[12–14,53] In fact, Lebens-Higgins *et al.* recently performed a systematic study on several common Li-ion cath-

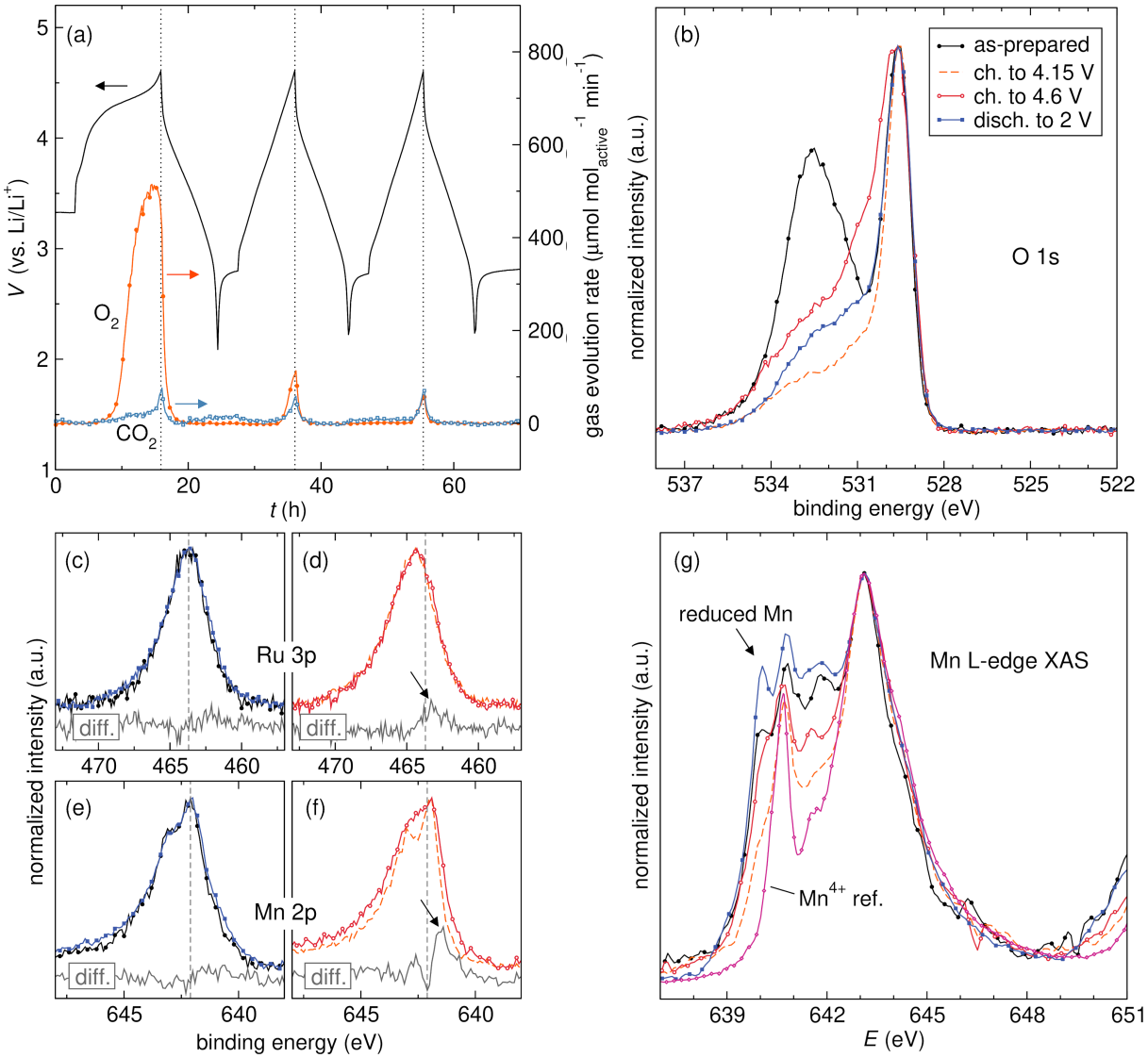

Figure 3: (a) *Operando* DEMS of $Li_2Ru_{0.3}Mn_{0.7}O_3$ for the first three cycles. (b) HAXPES at various SOC in the (b) O 1s, (c, d) Ru 3p, and (e, f) Mn 2p regions. (g) Mn L-edge XAS collected in total electron yield mode.

ode materials and observed the new feature, but it is instead attributed to transition metal reduction and electrolyte decomposition near the surface.[55] The same concepts are invoked here and are supported by HAXPES in the Ru 3p and Mn 2p region and XAS (TEY) at the Mn L-edge (Figure 3c-g). HAXPES results in the Ru 3p region closely mirror the K-edge XAS data with an initial positive shift at 4.15 V (Ru^{4+} to Ru^{5+}) and no further shift at 4.6 V. However, additional spectral weight arises at low binding energies in the fully charged vs. partially charged samples, suggesting a small proportion of reduced Ru near the surface upon oxidation. The Mn 2p HAXPES data, specifically comparing cathodes charged to 4.15 and 4.6 V (Figure 3f), show additional spectral weight (more substantial than the Ru case) at low binding energies in the fully charged sample as illustrated by the difference curve. This result indicates reduction of Mn near the surface at high voltages. Greater amounts of reduced Mn are also observed at high voltages in the Mn L-edge XAS (Figure 3g). Reduced Mn near the surface has been observed in a variety of Li-rich NMC materials,[49,50,56,57] which are structurally similar to $Li_2Ru_{0.3}Mn_{0.7}O_3$. O_2 gas release from the lattice near the surface has been shown to be accompanied by transition metal reduction and sometimes densification.[49,50,58–61]

The signs of reduced transition metals near the

surface in $Li_2Ru_{0.3}Mn_{0.7}O_3$ from HAXPES are not maintained upon discharge. To determine if the reduced metals are lost to the electrolyte, inductively coupled plasma mass spectrometry (ICP-MS) is performed for the electrolyte before and after cycling. Mn is observed in the electrolyte after cycling (Table S2) pointing to Mn dissolution, which has been observed in Mn-rich materials with low-valent Mn.[62–65] It is known that, in general, metal-oxygen bonding will be more rigid for metals with more covalent interactions.[refs] As such, it tracks that low-valent Mn, which is comparatively ionic in its interactions with O, could be mobile upon introduction of a widespread vacancy network during delithiation. The Mn L-edge XAS (TEY) results show the most significant quantity of reduced Mn in the fully discharged sample. As such, we assert that transition metals are reduced past the formal charge state of the pristine material on both the surface and in the bulk upon discharge. This result is consistent with the nucleation and growth model for spinel formation reported by Gu *et al.* in *C*2/*m* $Li_{1.2}Ni_{0.1}Mn_{0.525}Co_{0.175}O_2$,[49] where here we consider spinel formation as a proxy for reduction of transition metals and do not claim one way or the other if a spinel phase is forming in $Li_2Ru_{0.3}Mn_{0.7}O_3$.

To understand how the dynamic charge compensation and gas release affects local structure, extended X-ray absorption fine structure (EXAFS) analysis is performed and first- and second-shell bond lengths and correlation distances are extracted from fits. A summary of the fits of the EXAFS data is shown in Figure 4a-b S9 and the data and fits can be found in Figures S9 and S10 and S11 with additional analysis in Figure S12. Overall, the amplitude of the EXAFS decreases during charge and is not fully recovered upon discharge, indicating permanent increases in disorder .[11,19] The first-shell correlations correspond to consistent with metal migration and O loss.[11,19] *M*–O bonds (Figure 4a). Here, the *M*–O distance can be thought of as a proxy for redox involvement; that is, a shortening indicates oxidation and a lengthening indicates reduction. As expected, the Ru–O bond length shortens with oxidation at 4.15 V and lengthens slightly at 4.6 V, corroborating HAXPES results suggesting slightly reduced Ru when fully charged. After discharge, the Ru–O bond length has increased beyond that in the as-prepared sample, consistent with reduction beyond the formal oxidation state in the pristine phase. The Mn–O bond length does not change much with cycling, which highlights the relative redox inactivity in early cycles. A slight decrease in the Mn–O bond length is observed at 4.6 V, however, which supports the presence of reduced Mn as indicated by the XANES and HAXPES.

The second-shell coordination sphere is dominated by metal-metal scattering events. Li correlations are ignored in the model due to the small X-ray scattering cross section. The multi-structure model allows for metal-metal correlation lengths to be extracted for Ru and Mn back-scatterers from both Ru and Mn absorbers. For ease of understanding, correlations will be discussed with a M_1–M_2 convention where M_1 is the absorber -O and M_2 is the back-scatterer. The Ru–Ru correlation length decreases during the first oxidation, consistent with an overall lattice contraction (Figure 4b). Upon discharging, the Ru–Ru distance returns to the same value as in the as-prepared sample (approximately 3.03 Å). On cycle 2, Ru–Ru correlations contract during oxidation and expand again during reduction to comparable values as in the first cycle. However, by cycle 10, the correlation length at fully charged dips to 2.89 Å, a 0.14 Ådecrease, and only lengthens slightly to 2.92 Åduring discharge. Additionally, the model fits Ru–Ru correlations worse as $Li_2Ru_{0.3}Mn_{0.7}O_3$ is cycled (see relative errors) , suggesting significant changes to the Ru network with cycling. Ru–Mn correlations show less change overall due to the majority of Mn being redox inactive Mn^{4+}. However, as K-edge XAS and HAXPES show, more Mn is reduced with cycling. The redox involvement of Mn is supported by shorter Ru–Mn correlation lengths on cycle 10. Interestingly, on cycles 1 and 2, Ru–Ru and Ru–Mn correlation lengths converge at full charge , and by cycle 10 are almost identical. One possible explanation for this behavior is mobile Mn as has been observed in similar Li-rich NMC materials.[49,50,61,66] -*M* (*M* = Ru or Mn) correlations highlight the dynamic charge compensation mechanism and corroborate over-reduction of transition metals. An extended

discussion of the EXAFS results can be found in the SI.

~~The trends observed in the Mn–Mn correlations are similar to those with a Ru absorber (Figure 4b). The Mn–Mn correlation distance does not noticeably change during cycling, which is attributed to the large amount of Mn relative to Ru and a large proportion of the Mn being surrounded only by Mn and remaining relatively inert during cycling. Mn–Ru correlation distances trend the same as the fit Ru-Mn distances from the Ru K-edge EXAFS as expected. The errors are much larger due to Mn-Ru scattering events being a much smaller proportion of the overall scattering than Ru-Mn scattering events are to the Ru EXAFS . A comparison is shown in Figure S11. The changes suggest a reordering of Mn in the lattice during the first cycle, supporting the mobility of Mn during oxidation. These results also indicate that most changes to Mn are occurring in those that have redox active Ru next-nearest neighbors.~~

~~Significant changes to the Ru environments and Mn network in $Li_2Ru_{0.3}Mn_{0.7}O_3$ as evidenced by EXAFS are also observed by Raman spectroscopy~~ Raman spectroscopy provides an additional structural probe. The *ex situ* Raman spectra of $Li_2Ru_{0.3}Mn_{0.7}O_3$ and Li_2MnO_3 are shown in Figure 4d. The spectrum of Li_2MnO_3 is reported and the mode at 612 cm^{-1} is attributed to the MnO_6 A_{1g} symmetric stretch.[67] The lower frequency peaks are attributed to various Mn–O and Li–O modes. The spectrum of $Li_2Ru_{0.3}Mn_{0.7}O_3$ shows modes at similar frequencies with several key differences. First, the MnO_6 A_{1g} mode is significantly broader, which is attributed to a variety of different next nearest neighbor Mn environments. Two notable new modes at 678 and 718 cm^{-1} are observed and we attribute them to Ru–O related vibrations. *Ex situ* Raman spectra of several members of the $Li_2Ru_{1-y}Mn_yO_3$ ($y > 0.4$) solid solution further support the assignment as these modes increase in intensity relative to the Mn–O A_{1g} mode with increasing Ru content (Figure S3). Phonon modes calculated by Ponosov *et al.* for Li_2RuO_3 have good agreement with the two new modes in $Li_2Ru_{0.3}Mn_{0.7}O_3$, specifically those calculated at 551 cm^{-1} (A_g) and 677 cm^{-1} (A_g) were observed experimentally at 675 cm^{-1} and 715 cm^{-1}, respectively.[68] The atom displacement vectors associated with the calculated modes by Ponosov *et al.* are shown in Figure 4e-f.[68] Both new modes in $Li_2Ru_{0.3}Mn_{0.7}O_3$ have components of O translation that shortens one RuO_6 octahedral edge and brings two adjacent O closer together, and the lower frequency mode has a larger component of Ru motion. The presence of these modes and good agreement of the observed frequencies with Li_2RuO_3 may indicate Ru clustering.

Operando Raman spectroscopy is collected during a cyclic voltammetry measurement for three cycles to observe how these modes change with oxidation and reduction (Figure 4g-h). Galvanostatic cycling is not used due to the long times spent at high voltages that result in significant O_2 release and side reactions, which block Raman signal from the bulk material. Results show significant changes to the local structure with cycling. Upon charging, the Mn-related modes lose intensity and red-shift to lower frequencies, which supports the reduction of Mn as a result of O_2 release at high voltages. Additionally, a new potential-dependent mode at 682 cm^{-1} appears on the first negative scan. The mode is likely a sharp increase in intensity and blue-shift of the Ru–O related mode due to Ru oxidation because the Ru–O related mode decreases in intensity. The high-frequency Ru–O related mode also blue-shifts but to a lesser degree, which tracks with Ru motion being of lesser magnitude as shown in the calculated phonon mode. When the cyclic voltammogram reaches reduction, i.e. negative current, the changes begin to reverse. The point at which the CV switches from oxidation to reduction, and vice versa, are indicated with dashed lines in Figure 4g-h. However, the Mn-related modes do not recover their original intensity, indicating permanent changes to the Mn network. Selected spectra from the first cycle can be found in Figure S12 to more clearly show changes as a function of voltage. It is worth noting that we do not observe features previously reported to correspond to peroxo-like species,[69–73] and the sharp modes seen in all spectra in Figure S13 around 900 cm^{-1} are attributed to the electrolyte. On subsequent cycles, the Ru-related modes display similar behavior to that observed on the first cycle, indicating some reversibility with respect to the Ru local environment.

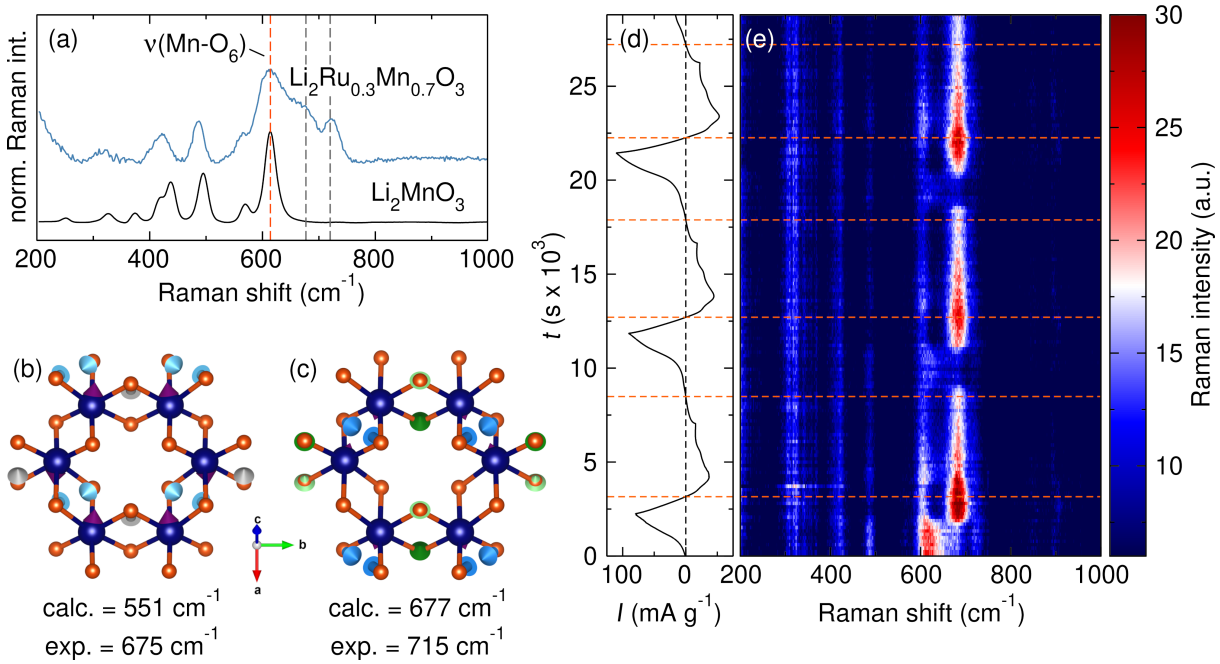

Figure 4: (a) ~~First shell metal-O bond lengths and (b) second shell metal-metal coordination distances as a function of cycling from EXAFS fits. (c)~~ *Ex situ* Raman spectroscopy of $Li_2Ru_{0.3}Mn_{0.7}O_3$ as compared to Li_2MnO_3 with the Mn-O A_{1g} mode and two new modes in $Li_2Ru_{0.3}Mn_{0.7}O_3$ highlighted. Calculated Raman modes in Li_2RuO_3 with translation vectors scaled up by a factor of 2, provided by authors from Ref. 62, at (~~d~~b) 551 cm^{-1} (predicted)/675 cm^{-1} (experimental) and (~~e~~c) 677 cm^{-1} (predicted)/715 cm^{-1} (experimental). (~~f~~d, ~~g~~e) *Operando* Raman spectroscopy of $Li_2Ru_{0.3}Mn_{0.7}O_3$ over three CV cycles with the zero current points marked with dotted lines to separate oxidative and reductive current regions.

$Li_2Ru_{0.3}Mn_{0.7}O_3$ shows a complex charge compensation mechanism that changes with cycling. On the first charge, XAS confirms that Ru is oxidized to Ru^{5+} and no further, which only accounts for 0.3 of the >1 Li that appears to be removed. Excess charge is accommodated by lattice O oxidation, but most of the anion oxidation is irreversible and results in significant O_2 gas release as shown by DEMS. O loss causes reduction of both Ru and Mn even in the charged material. Upon discharge, ~~both Mn and Ru are reduced~~ Ru is reduced in the bulk beyond the formal oxidation state of ~~the pristine material~~ 4+ as in the as-prepared material while Mn is reduced primarily near the surface where O loss is occurring. Importantly, Ru is found to undergo significant over-reduction throughout the bulk on the first cycle while Mn is more gradually reduced over many cycles, after which the transition metals are primarily responsible for charge compensation with very limited reversible O redox. ~~In subsequent cycles, the majority of the capacity is attributed to Ru and Mn redox alone, though the contributions from each change with time.~~ This dynamic redox behavior can give a false impression of good cyclability based on anion redox when, in fact, $Li_2Ru_{0.3}Mn_{0.7}O_3$ only exhibits significant contributions from O on the first charge cycle despite being within a solid solution ($Li_2Ru_{1-y}Mn_yO_3$) reported to have reversible anion redox.[12] Therefore, it is prudent to consider each material across a solid solution separately, especially when the end members have different structures and electrochemical behaviors. Considering $Li_2Ru_{0.3}Mn_{0.7}O_3$ with respect to Li_2MnO_3, this work shows that a small amount of a redox active metal activates semi-reversible Li removal and insertion (approximately 0.8 Li reversibly in this case) whereas all observed capacity in Li_2MnO_3 is from decomposition reactions and not Li cycling.[11] Nevertheless, the charge compensation mechanism is convoluted and changes with cycling, which highlights the difficulty of characterizing the long-term viability of anion redox materials based on Li-rich layered structures.

Acknowledgement This work was supported as part of the Center for Synthetic Control Across Length-scales for Advancing Rechargeables (SCALAR), an Energy Frontier Research Center funded by the U.S. Department of Energy, Office of Science, Basic Energy Sciences under Award No. DE-SC0019381. J. J. Z. acknowledges support from the National Science Foundation Graduate Research Fellowship under Grant No. (DGE-1745301). Use of the Advanced Photon Source at Argonne National Laboratory was supported by the U.S. Department of Energy, Office of Science, Office of Basic Energy Sciences, under Contract No. DE-AC02-06CH11357. We thank Wanli Yang and Tien-Lin Lee for assistance with the RIXS and HAXPES experiments, respectively. The ALS was supported by the U.S. Department of Energy, Office of Science, Basic Energy Sciences under contract No. DE-AC02-05CH11231. The authors acknowledge Diamond Light Source for time on Beamline I09 under Proposal SI127494. Inductively-Coupled Plasma Mass Spectrometry was performed in the Resnick Sustainability Institute's Water and Environment Lab at the California Institute of Technology.

Supporting Information Available

Experimental procedures, XRD patterns with Rietveld refinements with and without allowing intralayer mixing, table of structural parameters from Rietveld refinements, table of values from ICP-MS on electrolyte, *ex situ* Raman measurements, extended cycling electrochemical profiles, Ru and Mn K-edge XAS pre-edge features, O K-edge RIXS maps, TEY O K-edge XAS, Ru and Mn K-edge EXAFS with fits, selected Raman spectra from the first cycle of *operando* measurement, graphic of the custom spectroelectrochemical cell.

References

(1) Rozier, P.; Tarascon, J. M. Review—Li-Rich Layered Oxide Cathodes for Next-Generation Li-Ion Batteries: Chances and Challenges. *J. Electrochem. Soc.* **2015**, *162*, A2490–A2499.

(2) Grimaud, A.; Hong, W. T.; Shao-Horn, Y.; Tarascon, J.-M. Anionic Redox Processes for Electrochemical Devices. *Nat. Mater.* **2016**, *15*, 121–126.

(3) Li, B.; Xia, D. Anionic Redox in Rechargeable Lithium Batteries. *Adv. Mater.* **2017**, *29*, 1701054.

(4) Assat, G.; Tarascon, J.-M. Fundamental Understanding and Practical Challenges of Anionic Redox Activity in Li-ion Batteries. *Nat. Energy* **2018**, *3*, 373–386.

(5) Hu, S.; Pillai, A. S.; Liang, G.; Pang, W. K.; Wang, H.; Li, Q.; Guo, Z. Li-Rich Layered Oxides and Their Practical Challenges: Recent Progress and Perspectives. *Electrochem. Energ. Rev.* **2019**, *2*, 277–311.

(6) Yang, J.; Niu, Y.; Wang, X.; Xu, M. A Review on the Electrochemical Reaction of Li-rich Layered Oxide Materials. *Inorg. Chem. Front.* **2021**, *8*, 4300–4312.

(7) Nitta, N.; Wu, F.; Lee, J. T.; Yushin, G. Li-Ion Battery Materials: Present and Future. *Mater. Today* **2015**, *18*, 252–264.

(8) M. Thackeray, M.; Kang, S.-H.; S. Johnson, C.; T. Vaughey, J.; Benedek, R.; A. Hackney, S. Li_2MnO_3-Stabilized $LiMO_2$ (M = Mn, Ni, Co) Electrodes for Lithium-Ion Batteries. *J. Mater. Chem.* **2007**, *17*, 3112–3125.

(9) Thackeray, M. M. Manganese Oxides for Lithium Batteries. *Prog. Solid State Ch.* **1997**, *25*, 1–71.

(10) Robertson, A. D.; Bruce, P. G. Mechanism of Electrochemical Activity in Li_2MnO_3. *Chem. Mater.* **2003**, *15*, 1984–1992.

(11) Rana, J.; Papp, J. K.; Lebens-Higgins, Z.; Zuba, M.; Kaufman, L. A.; Goel, A.; Schmuch, R.; Winter, M.; Whittingham, M. S.; Yang, W.; McCloskey, B. D.; Piper, L. F. J. Quantifying the Capacity Contributions during Activation of Li_2MnO_3. *ACS Energy Lett.* **2020**, *5*, 634–641.

(12) Sathiya, M.; Ramesha, K.; Rousse, G.; Foix, D.; Gonbeau, D.; Prakash, A. S.; Doublet, M. L.; Hemalatha, K.; Tarascon, J.-M. High Performance $Li_2Ru_{1-y}Mn_yO_3$ ($0.2 \leq y \leq 0.8$) Cathode Materials for Rechargeable Lithium-Ion Batteries: Their Understanding. *Chem. Mater.* **2013**, *25*, 1121–1131.

(13) Sathiya, M.; Rousse, G.; Ramesha, K.; Laisa, C. P.; Vezin, H.; Sougrati, M. T.; Doublet, M.-L.; Foix, D.; Gonbeau, D.; Walker, W.; Prakash, A. S.; Hassine, M. B.; Dupont, L.; Tarascon, J.-M. Reversible Anionic Redox Chemistry in High-Capacity Layered-Oxide Electrodes. *Nat. Mater.* **2013**, *12*, 827.

(14) McCalla, E.; Abakumov, A. M.; Saubanère, M.; Foix, D.; Berg, E. J.; Rousse, G.; Doublet, M.-L.; Gonbeau, D.; Novák, P.; Van Tendeloo, G.; Dominko, R.; Tarascon, J.-M. Visualization of O-O Peroxo-like Dimers in High-Capacity Layered Oxides for Li-ion Batteries. *Science* **2015**, *350*, 1516–1521.

(15) Pearce, P. E.; Perez, A. J.; Rousse, G.; Saubanère, M.; Batuk, D.; Foix, D.; McCalla, E.; Abakumov, A. M.; Tendeloo, G. V.; Doublet, M.-L.; Tarascon, J.-M. Evidence for Anionic Redox Activity in a Tridimensional-Ordered Li-rich Positive Electrode β-Li_2IrO_3. *Nat. Mater.* **2017**, *16*, 580.

(16) James, A. C. W. P.; Goodenough, J. B. Structure and Bonding in Lithium Ruthenate, Li_2RuO_3. *J. Solid State Chem.* **1988**, *74*, 287–294.

(17) Li, B.; Shao, R.; Yan, H.; An, L.; Zhang, B.; Wei, H.; Ma, J.; Xia, D.; Han, X. Understanding the Stability for Li-Rich Layered Oxide Li_2RuO_3 Cathode. *Adv. Funct. Mater.* **2016**, *26*, 1330–1337.

(18) Sathiya, M.; Abakumov, A. M.; Foix, D.; Rousse, G.; Ramesha, K.; Saubanère, M.; Doublet, M. L.; Vezin, H.; Laisa, C. P.; Prakash, A. S.; Gonbeau, D.; VanTendeloo, G.; Tarascon, J.-M. Origin of Voltage Decay in High-Capacity Layered Oxide Electrodes. *Nat. Mater.* **2015**, *14*, 230–238.

(19) Lyu, Y.; Hu, E.; Xiao, D.; Wang, Y.; Yu, X.; Xu, G.; Ehrlich, S. N.; Amine, K.; Gu, L.; Yang, X.-Q.; Li, H. Correlations between Transition-Metal Chemistry, Local Structure, and Global Structure in $Li_2Ru_{0.5}Mn_{0.5}O_3$ Investigated in a Wide Voltage Window. *Chem. Mater.* **2017**, *29*, 9053–9065.

(20) Kobayashi, H.; Kanno, R.; Kawamoto, Y.; Tabuchi, M.; Nakamura, O. Physical Properties of the De-Lithiated $Li_{2-x}RuO_3$ with the Layered Structure. *Solid State Ion.* **1996**, *86–88*, 859–863.

(21) Chen, Y.-C.; Huo, M.; Liu, Y.; Chen, T.; Leng, C.-C.; Li, Q.; Sun, Z.-L.; Song, L.-J. Structural, Electrical, and Lithium Ion Dynamics of Li_2MnO_3 from Density Functional Theory. *Chin. Phys. Lett.* **2015**, *32*, 017102.

(22) Boulineau, A.; Croguennec, L.; Delmas, C.; Weill, F. Reinvestigation of Li_2MnO_3 Structure: Electron Diffraction and High Reso-

lution TEM. *Chem. Mater.* **2009**, *21*, 4216–4222.

(23) Boulineau, A.; Croguennec, L.; Delmas, C.; Weill, F. Structure of Li_2MnO_3 with Different Degrees of Defects. *Solid State Ion.* **2010**, *180*, 1652–1659.

(24) Wang, Y.; Gu, H.-T.; Song, J.-H.; Feng, Z.-H.; Zhou, X.-B.; Zhou, Y.-N.; Wang, K.; Xie, J.-Y. Suppressing Mn Reduction of Li-Rich Mn-Based Cathodes by F-Doping for Advanced Lithium-Ion Batteries. *J. Phys. Chem. C* **2018**, *122*, 27836–27842.

(25) J. Carroll, K.; Qian, D.; Fell, C.; Calvin, S.; M. Veith, G.; Chi, M.; Baggetto, L.; Shirley Meng, Y. Probing the Electrode/Electrolyte Interface in the Lithium Excess Layered Oxide $Li_{1.2}Ni_{0.2}Mn_{0.6}O_2$. *Phys. Chem. Chem. Phys.* **2013**, *15*, 11128–11138.

(26) Shimoda, K.; Minato, T.; Nakanishi, K.; Komatsu, H.; Matsunaga, T.; Tanida, H.; Arai, H.; Ukyo, Y.; Uchimoto, Y.; Ogumi, Z. Oxidation Behaviour of Lattice Oxygen in Li-rich Manganese-Based Layered Oxide Studied by Hard X-ray Photoelectron Spectroscopy. *J. Mater. Chem. A* **2016**, *4*, 5909–5916.

(27) Mizushima, K.; Jones, P. C.; Wiseman, P. J.; Goodenough, J. B. Li_xCoO_2 (0<x<-1): A new cathode material for batteries of high energy density. *Mater. Res. Bull.* **1980**, *15*, 783–789.

(28) Xu, J.; Sun, M.; Qiao, R.; Renfrew, S. E.; Ma, L.; Wu, T.; Hwang, S.; Nordlund, D.; Su, D.; Amine, K.; Lu, J.; McCloskey, B. D.; Yang, W.; Tong, W. Elucidating Anionic Oxygen Activity in Lithium-Rich Layered Oxides. *Nat. Commun.* **2018**, *9*, 947.

(29) Baker, M. L.; Mara, M. W.; Yan, J. J.; Hodgson, K. O.; Hedman, B.; Solomon, E. I. K- and L-edge X-ray Absorption Spectroscopy (XAS) and Resonant Inelastic X-ray Scattering (RIXS) Determination of Differential Orbital Covalency (DOC) of Transition Metal Sites. *Coord. Chem. Rev.* **2017**, *345*, 182–208.

(30) Zhuo, Z.; Dai, K.; Wu, J.; Zhang, L.; Tamura, N.; Chuang, Y.-d.; Feng, J.; Guo, J.; Shen, Z.-x.; Liu, G.; Pan, F.; Yang, W. Distinct Oxygen Redox Activities in Li_2MO_3 (M = Mn, Ru, Ir). *ACS Energy Lett.* **2021**, *6*, 3417–3424.

(31) Assat, G.; Iadecola, A.; Foix, D.; Dedryvère, R.; Tarascon, J.-M. Direct Quantification of Anionic Redox over Long Cycling of Li-Rich NMC via Hard X-ray Photoemission Spectroscopy. *ACS Energy Lett.* **2018**, *3*, 2721–2728.

(32) Hu, E.; Yu, X.; Lin, R.; Bi, X.; Lu, J.; Bak, S.; Nam, K.-W.; Xin, H. L.; Jaye, C.; Fischer, D. A.; Amine, K.; Yang, X.-Q. Evolution of Redox Couples in Li- and Mn-rich Cathode Materials and Mitigation of Voltage Fade by Reducing Oxygen Release. *Nat Energy* **2018**, *3*, 690–698.

(33) Renfrew, S. E.; McCloskey, B. D. Residual Lithium Carbonate Predominantly Accounts for First Cycle CO_2 and CO Outgassing of Li-Stoichiometric and Li-Rich Layered Transition-Metal Oxides. *J. Am. Chem. Soc.* **2017**, *139*, 17853–17860.

(34) Qiu, B.; Zhang, M.; Wu, L.; Wang, J.; Xia, Y.; Qian, D.; Liu, H.; Hy, S.; Chen, Y.; An, K.; Zhu, Y.; Liu, Z.; Meng, Y. S. Gas–Solid Interfacial Modification of Oxygen Activity in Layered Oxide Cathodes for Lithium-Ion Batteries. *Nat Commun* **2016**, *7*, 12108.

(35) Liang, Y.; Prendergast, D. Quantum Many-Body Effects in X-Ray Spectra Efficiently Computed Using a Basic Graph Algorithm. *Phys. Rev. B* **2018**, *97*, 205127.

(36) Luo, K.; Roberts, M. R.; Hao, R.; Guerrini, N.; Pickup, D. M.; Liu, Y.-S.; Edström, K.; Guo, J.; Chadwick, A. V.; Duda, L. C.; Bruce, P. G. Charge-Compensation in 3d-Transition-Metal-Oxide Intercalation Cathodes through the Generation of Localized Electron Holes on Oxygen. *Nat. Chem.* **2016**, *8*, 684.

(37) Gent, W. E. et al. Coupling between Oxygen Redox and Cation Migration Explains Unusual Electrochemistry in Lithium-Rich Layered Oxides. *Nat. Commun.* **2017**, *8*, 2091.

(38) Lebens-Higgins, Z. W.; Vinckeviciute, J.; Wu, J.; Faenza, N. V.; Li, Y.; Sallis, S.; Pereira, N.; Meng, Y. S.; Amatucci, G. G.; Der Ven, A. V.; Yang, W.; Piper, L. F. J. Distinction between Intrinsic and X-ray-Induced Oxidized Oxygen States in Li-Rich 3d Layered Oxides and $LiAlO_2$. *J. Phys. Chem. C* **2019**, *123*, 13201–13207.

(39) House, R. A.; Marie, J.-J.; Park, J.; Rees, G. J.; Agrestini, S.; Nag, A.; Garcia-Fernandez, M.; Zhou, K.-J.; Bruce, P. G. Covalency Does Not Suppress O2 Formation in 4d and 5d Li-rich O-redox Cathodes. *Nat. Commun.* **2021**, *12*, 2975.

(40) House, R. A.; Rees, G. J.; Pérez-Osorio, M. A.; Marie, J.-J.; Boivin, E.; Robertson, A. W.; Nag, A.; Garcia-Fernandez, M.; Zhou, K.-J.; Bruce, P. G. First-Cycle Voltage Hysteresis in Li-rich 3d Cathodes Associated with Molecular O_2 Trapped in the Bulk. *Nat. Energy* **2020**, *5*, 777–785.

(41) House, R. A.; Maitra, U.; Pérez-Osorio, M. A.; Lozano, J. G.; Jin, L.; Somerville, J. W.; Duda, L. C.; Nag, A.; Walters, A.; Zhou, K.-J.; Roberts, M. R.; Bruce, P. G. Superstructure Control of First-Cycle Voltage Hysteresis in Oxygen-Redox Cathodes. *Nature* **2020**, *577*, 502–508.

(51) Qiao, R.; Chuang, Y.-D.; Yan, .

(48) Renfrew, S.; Yang, W. Soft X-Ray Irradiation Effects E.; McCloskey, B. D. Quantification of Li_2O_2Surface Oxygen Depletion , $Li_2CO_3$and Li_2O RevealedSolid Carbonate Evolution by on the Absorption SpectroscopyFirst Cycle . of $LiNi_{0.6}Mn_{0.2}Co_{0.2}O_2$ Electrodes. *PLoS One**ACS Appl. Energy Mater.* **2012****2019**, *7*2, e491823762–3772.

(52) Risthaus, T.; Zhou, D.; Cao, X.; He, X.; Qiu, B.; Wang, J. ; Zhang, L.; Liu, Z.; Paillard, E.; Schumacher, G.; Winter, M.; Li, J. A High-Capacity P2 $Na_{2/3}Ni_{1/3}Mn_{2/3}O_2$ Cathode Material for Sodium Ion Batteries with Oxygen Activity. .

(45) Kaufman, L. A.; McCloskey, B. D. Surface Lithium Carbonate Influences Electrolyte Degradation via Reactive Oxygen Attack in Lithium-Excess Cathode Materials. *JChem. Power SourcesMater.* **20182021**, *395*33, 16–244170–4176.

(46) Armstrong, A. R.; Holzapfel, M.; Novák, P.; Johnson, C. S.; Kang, S.-H.; Thackeray, M. M.; Bruce, P. G. Demonstrating Oxygen Loss and Associated Structural Reorganization in the Lithium Battery Cathode $Li[Ni_{0.2}Li_{0.2}Mn_{0.6}0.6]O_2$. *J. Am. Chem. Soc.* **2006**, *128*, 8694–8698.

(47) McCalla, E. et al. Reversible Li-Intercalation through Oxygen Reactivity in Li-Rich Li-Fe-Te Oxide Materials. *J. Electrochem. Soc.* **2015**, *162*, A1341–A1351.

(48) Renfrew, S. E.; McCloskey, B. D. Quantification of Surface Oxygen Depletionand Solid Carbonate Evolutionon the First Cycleof $LiNi_{0.6}Mn_{0.2}Co_{0.2}O_2$ Electrodes. *ACS Appl. Energy Mater.* **2019**, *2*, 3762–3772McCloskey]kaufmanSurfaceLithiumCarbona Kaufman, L. A.; McCloskey, B. D. Surface Lithium Carbonate Influences Electrolyte Degradationvia Reactive Oxygen Attackin Lithium-Excess Cathode Materials. *Chem. Mater.* **2021**, *33*, 4170–4176.

(49) Gu, M.; Belharouak, I.; Zheng, J.; Wu, H.; Xiao, J.; Genc, A.; Amine, K.; Thevuthasan, S.; Baer, D. R.; Zhang, J.-G.; Browning, N. D.; Liu, J.; Wang, C. Formation of the Spinel Phase in the Layered Composite Cathode Used in Li-Ion Batteries. *ACS Nano* **2013**, *7*, 760–767.

(50) Bak, S.-M.; Hu, E.; Zhou, Y.; Yu, X.; Senanayake, S. D.; Cho, S.-J.; Kim, K.-B.;

Chung, K. Y.; Yang, X.-Q.; Nam, K.-W. Structural Changes and Thermal Stability of Charged $LiNi_xMn_yCo_zO_2$ Cathode Materials Studied by Combined In Situ Time-Resolved XRD and Mass Spectroscopy. *ACS Appl. Mater. Interfaces* **2014**, *6*, 22594–22601.

(51) Qiao, R.; Chuang, Y.-D.; Yan, S.; Yang, W. Soft X-Ray Irradiation Effects of Li_2O_2, Li_2CO_3 and Li_2O Revealed by Absorption Spectroscopy. *PLOS ONE* **2012**, *7*, e49182.

(52) Risthaus, T.; Zhou, D.; Cao, X.; He, X.; Qiu, B.; Wang, J.; Zhang, L.; Liu, Z.; Paillard, E.; Schumacher, G.; Winter, M.; Li, J. A High-Capacity P2 $Na_{2/3}Ni_{1/3}Mn_{2/3}O_2$ Cathode Material for Sodium Ion Batteries with Oxygen Activity. *J. Power Sources* **2018**, *395*, 16–24.

(53) Foix, D.; Sathiya, M.; McCalla, E.; Tarascon, J.-M.; Gonbeau, D. X-Ray Photoemission Spectroscopy Study of Cationic and Anionic Redox Processes in High-Capacity Li-Ion Battery Layered-Oxide Electrodes. *J. Phys. Chem. C* **2016**, *120*, 862–874.

(54) Dahéron, L.; Dedryvère, R.; Martinez, H.; Ménétrier, M.; Denage, C.; Delmas, C.; Gonbeau, D. Electron Transfer Mechanisms upon Lithium Deintercalation from $LiCoO_2$ to CoO_2 Investigated by XPS. *Chem. Mater.* **2008**, *20*, 583–590.

(55) Lebens-Higgins, Z. W.; Chung, H.; Zuba, M. J.; Rana, J.; Li, Y.; Faenza, N. V.; Pereira, N.; McCloskey, B. D.; Rodolakis, F.; Yang, W.; Whittingham, M. S.; Amatucci, G. G.; Meng, Y. S.; Lee, T.-L.; Piper, L. F. J. How Bulk Sensitive Is Hard X-ray Photoelectron Spectroscopy: Accounting for the Cathode–Electrolyte Interface When Addressing Oxygen Redox. *J. Phys. Chem. Lett.* **2020**, *11*, 2106–2112.

(56) Reed, J.; Ceder, G.; Ven, A. V. D. Layered-to-Spinel Phase Transition in Li_xMnO_2. *Electrochem. Solid-State Lett.* **2001**, *4*, A78.

(57) Jarvis, K.; Wang, C.-C.; Varela, M.; Unocic, R. R.; Manthiram, A.; Ferreira, P. J. Surface Reconstruction in Li-Rich Layered Oxides of Li-Ion Batteries. *Chem. Mater.* **2017**, *29*, 7668–7674.

(58) Boulineau, A.; Simonin, L.; Colin, J.-F.; Bourbon, C.; Patoux, S. First Evidence of Manganese–Nickel Segregation and Densification upon Cycling in Li-Rich Layered Oxides for Lithium Batteries. *Nano Lett.* **2013**, *13*, 3857–3863.

(59) Koga, H.; Croguennec, L.; Ménétrier, M.; Mannessiez, P.; Weill, F.; Delmas, C. Different Oxygen Redox Participation for Bulk and Surface: A Possible Global Explanation for the Cycling Mechanism of $Li_{1.20}Mn_{0.54}Co_{0.13}Ni_{0.13}O_2$. *J. Power Sources* **2013**, *236*, 250–258.

(60) Zuo, W.; Luo, M.; Liu, X.; Wu, J.; Liu, H.; Li, J.; Winter, M.; Fu, R.; Yang, W.; Yang, Y. Li-Rich Cathodes for Rechargeable Li-based Batteries: Reaction Mechanisms and Advanced Characterization Techniques. *Energy Environ. Sci.* **2020**, *13*, 4450–4497.

(61) Chen, J. et al. Pseudo-Bonding and Electric-Field Harmony for Li-Rich Mn-Based Oxide Cathode. *Adv. Funct. Mater.* **2020**, *30*, 2004302.

(62) Zhu, Z.; Gao, R.; Waluyo, I.; Dong, Y.; Hunt, A.; Lee, J.; Li, J. Stabilized Co-Free Li-Rich Oxide Cathode Particles with An Artificial Surface Prereconstruction. *Adv. Energy Mater.* **2020**, *10*, 2001120.

(63) Wang, C.; Xing, L.; Vatamanu, J.; Chen, Z.; Lan, G.; Li, W.; Xu, K. Overlooked Electrolyte Destabilization by Manganese (II) in Lithium-Ion Batteries. *Nat. Commun.* **2019**, *10*, 3423.

(64) Wang, X.; Nakamura, H.; Yoshio, M. Capacity Fading Mechanism for Oxygen Defect Spinel as a 4 V Cathode Material in Li-ion Batteries. *J. Power Sources* **2002**, *110*, 19–26.

(65) Xia, Y.; Zhou, Y.; Yoshio, M. Capacity Fading on Cycling of 4 V $Li/LiMn_2O_4$ Cells. *J. Electrochem. Soc.* **1997**, *144*, 2593.

(66) Benedek, R.; Iddir, H. Simulation of First-Charge Oxygen-Dimerizationand Mn-Migrationin Li-Rich Layered Oxides $xLi_2MnO_3 \cdot (1-x)LiMO_2$and Implicationsfor Voltage Fade. *J. Phys. Chem. C* **2017**, *121*, 6492–6499.

(67) Yu, D. Y. W.; Yanagida, K. Structural Analysis of Li_2MnO_3 and Related Li-Mn-O Materials. *J. Electrochem. Soc.* **2011**, *158*, A1015–A1022.

(68) Ponosov, Y. S.; Komleva, E. V.; Streltsov, S. V. Phonon Anomalies near the Magnetostructural Transition in Li_2RuO_3: Raman Spectroscopy and Density Functional Theory Studies. *Phys. Rev. B* **2019**, *100*, 134310.

(69) Li, X.; Qiao, Y.; Guo, S.; Xu, Z.; Zhu, H.; Zhang, X.; Yuan, Y.; He, P.; Ishida, M.; Zhou, H. Direct Visualization of the Reversible O^{2-}/O^{-} Redox Process in Li-Rich Cathode Materials. *Adv. Mater.* **2018**, *30*, 1705197.

(70) Zhang, J.; Cheng, F.; Chou, S.; Wang, J.; Gu, L.; Wang, H.; Yoshikawa, H.; Lu, Y.; Chen, J. Tuning Oxygen Redox Chemistry in Li-Rich Mn-Based Layered Oxide Cathodes by Modulating Cation Arrangement. *Adv. Mater.* **2019**, *31*, 1901808.

(71) Ning, F.; Li, B.; Song, J.; Zuo, Y.; Shang, H.; Zhao, Z.; Yu, Z.; Chu, W.; Zhang, K.; Feng, G.; Wang, X.; Xia, D. Inhibition of Oxygen Dimerization by Local Symmetry Tuning in Li-rich Layered Oxides for Improved Stability. *Nat. Commun.* **2020**, *11*, 4973.

(72) Li, X.; Qiao, Y.; Guo, S.; Jiang, K.; Ishida, M.; Zhou, H. A New Type of Li-Rich Rock-Salt Oxide $Li_2Ni_{1/3}Ru_{2/3}O_3$ with Reversible Anionic Redox Chemistry. *Adv. Mater.* **2019**, *31*, 1807825.

(73) Qiao, Y.; Guo, S.; Zhu, K.; Liu, P.; Li, X.; Jiang, K.; Sun, C.-J.; Chen, M.; Zhou, H. Reversible Anionic Redox Activity in Na_3RuO_4 Cathodes: A Prototype Na-rich Layered Oxide. *Energy Environ. Sci.* **2018**, *11*, 299–305.

TOC Graphic

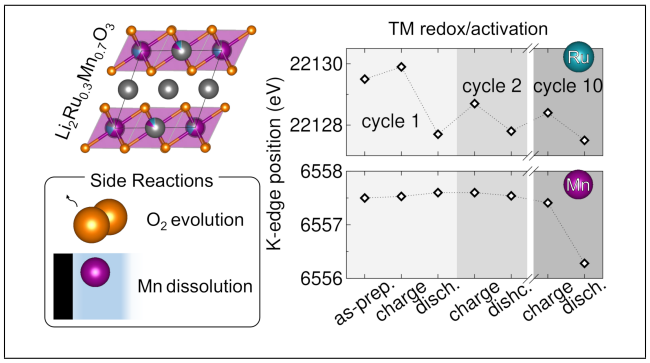
$Li_2Ru_{0.3}Mn_{0.7}O_3$
Side Reactions
O_2 evolution
Mn dissolution
TM redox/activation
K-edge position (eV)
22130
22128
6558
6557
6556
cycle 1
cycle 2
cycle 10
Ru
Mn
as-prep.
charge
disch.
charge
dishc.
charge
disch.